NEUROSCIENCE

Chronic alcohol induces subcircuit-specific striatonigral plasticity enhancing the sensorimotor basal ganglia role in action execution

Giacomo Sitzia[1,2], Sebastiano Bariselli[1,3], Alexa Gracias[1], David M. Lovinger[1]*

Functional deficits in basal ganglia (BG) circuits contribute to cognitive and motor dysfunctions in alcohol use disorder. Chronic alcohol exposure alters synaptic function and neuronal excitability in the dorsal striatum, but it remains unclear how it affects BG output that is mediated by the substantia nigra pars reticulata (SNr). Here, we describe a neuronal subpopulation-specific synaptic organization of striatal and subthalamic (STN) inputs to the medial and lateral SNr. Chronic alcohol exposure (CIE) potentiated dorsolateral striatum (DLS) inputs but did not change dorsomedial striatum and STN inputs to the SNr. Chemogenetic inhibition of DLS direct pathway neurons revealed an enhanced role for DLS direct pathway neurons in execution of an instrumental lever-pressing task. Overall, we reveal a subregion-specific organization of striatal and subthalamic inputs onto the medial and lateral SNr and find that potentiated DLS-SNr inputs are accompanied by altered BG control of action execution following CIE.

INTRODUCTION

Alcohol is one of the most abused drugs worldwide. Alcohol use disorder (AUD) is a disease characterized by loss of control over alcohol intake (*1*, *2*), with devastating consequences for the affected people and society. Alcohol can affect brain function through acute, direct interactions with multiple substrates including, but not limited to, neurotransmitter receptors (*3*, *4*). Alcohol also produces long-term changes in neural circuits (*3*, *5*), which contribute to long-term cognitive and motor dysfunctions. Therefore, disentangling the complexity of brain circuits and their susceptibility to alcohol effects is necessary to refine therapeutic strategies targeting behavioral dysfunctions in AUD.

Brain regions of the basal ganglia (BG) coordinate motor and non-motor behaviors based on the present context and past experiences (*6*–*9*), and their dysfunction has been implicated in the development of pathological habits and altered control of goal-directed behavior in AUD (*10*). BG circuits control diverse functional outputs through the GABAergic projection neurons of the substantia nigra pars reticulata (SNr) and the globus pallidus internal segment (GPi), which target brainstem, midbrain, and thalamic nuclei (*11*–*13*). The BG control the SNr via striatal GABAergic direct pathway inputs and subthalamic nucleus (STN) glutamatergic indirect pathway inputs, which, according to the classical view, are thought to promote or suppress behavioral outputs influenced by the SNr, respectively (*8*, *9*, *14*). The main neuronal population of the dorsal striatum (DS) is the spiny projection neurons (SPNs), divided into direct pathway SPNs (dSPNs) targeting the SNr/GPi and indirect pathway SPNs (iSPNs) targeting the globus pallidus external segment (GPe). The GPe, in turn, projects to the STN and the SNr. The direct and indirect pathways are a circuit backbone shared across anatomically parallel BG circuits with distinct functional roles (*15*–*17*). The dorsomedial (DMS) and dorsolateral (DLS) subregions of the striatum receive associative and sensorimotor cortical inputs

(*18*, *19*) and have been implicated in goal-directed (DMS) and habitual (DLS) action control (*6*). Striatal projections to the SNr are topographically organized; hence, spatially distinct subpopulations in the medial (^{M}SNr) and ventrolateral (^{L}SNr) SNr receive inputs from the DMS and DLS (*12*, *20*). Understanding how alcohol affects BG circuits requires a refined knowledge of the organization of synaptic inputs to subpopulations of SNr neurons.

The intrinsic physiological properties of SNr neurons vary along the mediolateral axis of the nucleus (*13*). Molecularly identified subpopulations of SNr neurons include a majority of parvalbumin-expressing (PV$^+$) neurons, enriched in the ventrolateral aspects of the nucleus, as well as other subpopulations that have been characterized on the basis of the expression of the vesicular GABA transporter (VGAT), calretinin, and glutamate decarboxylase 2 enzyme (GAD2) (*13*, *21*–*23*). The physiological properties and projection patterns of PV$^+$ SNr neurons differentiate them from other SNr neuron subpopulations (*21*, *24*). The molecular and functional heterogeneity of SNr neurons is also tuned to the diversity of neuronal targets innervated by the SNr (*13*). However, whether synaptic inputs to distinct SNr neuron subpopulations are organized to reflect their functional heterogeneity remains unclear.

The synaptic effects of acute and chronic alcohol exposure on the BG have been investigated in animal studies mainly focused on striatal circuits (*25*, *26*). These experiments showed that acute alcohol effects and maladaptive circuit adaptations following chronic alcohol exposure vary according to the striatal cell type, synaptic input, and subregion examined. In a series of seminal studies, Corbit *et al.* (*27*, *28*) demonstrated that the control of alcohol self-administration in rats shifts from goal-directed to habitual upon repeated (>2 weeks) exposure due to an increased engagement of the DLS over the DMS. Within the DLS, acute exposure of striatal slices to alcohol decreases GABAergic tone on SPNs inhibits SPN-SPN synapses and fast-spiking interneuron-SPN synapses (*29*). This suggests that acute alcohol exposure initiates a disinhibition of DLS circuits. Within the DMS, altered synaptic plasticity of the medial prefrontal cortex–DMS inputs contributes to perseveration in alcohol-seeking behaviors (*30*, *31*), whereas weakened orbitofrontal cortex–DMS inputs impairs goal-directed action control following chronic alcohol exposure (*32*, *33*). These studies indicate that chronic alcohol

[1]Laboratory for Integrative Neuroscience, National Institute on Alcohol Abuse and Alcoholism, National Institutes of Health, Rockville, MD, USA. [2]Department of Neuroscience, Faculty of Health and Medical Sciences, University of Copenhagen, Copenhagen, Denmark. [3]IRCCS Humanitas Research Hospital, Via Manzoni 56, 20089 Rozzano, Milan, Italy.
*Corresponding author. Email: lovindav@mail.nih.gov

exposure induces synaptic maladaptations in specific striatal subcircuits to cause distinct behavioral alterations. However, the susceptibility to alcohol effects of BG output structures downstream of the striatum remains poorly understood. This limits our understanding of the behavioral and circuit adaptations induced by chronic alcohol exposure.

Here, we asked whether synaptic plasticity in SNr contributes to altered control of action execution following chronic alcohol exposure in mice. First, we used optogenetics-assisted circuit mapping and found that DMS-SNr and DLS-SNr inputs differ in their presynaptic properties and target distinct SNr subpopulations. Moreover, we found that indirect pathway inputs from the STN are biased to the lateral SNr. We then demonstrated that chronic alcohol exposure potentiates DLS-SNr inputs without changing the strength and presynaptic properties of DMS-SNr and STN-SNr inputs. Last, we found that chemogenetic inhibition of DLS-SNr inputs impaired action execution in mice exposed to chronic alcohol but not in control mice. Overall, we identified a synaptic basis for an abnormal functional control of action execution in the sensorimotor BG circuit following chronic alcohol exposure.

RESULTS

Input-output organization of the DMS-SNr and DLS-SNr subcircuits

Our first goal was to establish the functional relationships between distinct striatal inputs and their targets in the SNr. We virally expressed the opsin Chronos in the DMS or DLS using injections of an adeno-associated virus (AAV) (pAAV5-Syn-Chronos-GFP) and performed ex vivo whole-cell patch-clamp recordings coupled with local field optogenetic stimulation in SNr slices (Fig. 1A). As expected, DMS-GFP[+] terminals were detected in the medial portion of the SNr ([M]SNr). In contrast, DLS-GFP[+] terminals were detected in the ventrolateral portion of the SNr ([L]SNr) (12, 16, 20) (Fig. 1A). Therefore, we focused our recordings on the [M]SNr to characterize DMS-SNr synapses and on the [L]SNr to characterize DLS-SNr synapses. The amplitude of optically-evoked inhibitory post-synaptic currents (oIPSCs) at DMS-[M]SNr (2.5 $\pm$ 0.6 nA) and DLS-[L]SNr (1.6 $\pm$ 0.4 nA) synapses was not statistically different (fig. S1A), while the oIPSC latency to peak was statistically different but consistent in both synapses with monosynaptic inputs (DMS-[M]SNr, 3.8 $\pm$ 0.1 ms; DLS-[L]SNr, 5.1 $\pm$ 0.2 ms) (fig. S1B). We compared the presynaptic properties of DMS-[M]SNr and DLS-[L]SNr synapses by calculating the paired-pulse ratio (PPR) using stimuli delivered with a 50-ms interpulse interval. We found that PPRs at DMS-SNr synapses were characterized by short-term depression (PPR, 0.87 $\pm$ 0.06), that PPRs at DLS-SNr synapses were characterized by short-term facilitation (PPR, 1.29 $\pm$ 0.12), and that overall PPRs were significantly different between the two synapses (Fig. 1B). This difference was further evidenced during a train of 10 stimuli delivered at 20 Hz (fig. S1C). These results indicate that DMS-[M]SNr and DLS-[L]SNr synapses differ in their presynaptic properties.

In a subset of these experiments, we used PVCre-TdTom mice to label PV^{+} SNr neurons, previously indicated as the major GABAergic subpopulation of the SNr (13, 24). We found a significantly higher proportion of TdTom^{−} neurons (PV[−]) among DMS-connected neurons (1 TdTom[+] and 10 TdTom[−]) compared to a majority of TdTom^{+} neurons (PV[+]) among DLS-connected neurons (8 TdTom[+] and 2 TdTom[−]) (Fig. 1C). This first series of experiments indicated that

the DMS and DLS target molecularly distinct subpopulations of SNr neurons. Next, we investigated how the firing activity of [M]SNr and [L]SNr neurons is controlled by their striatal inputs.

We used the same Chronos-assisted DMS-[M]SNr and DLS-[L]SNr circuit mapping strategy to perform current-clamp experiments identifying SNr neurons as DMS- or DLS-targeted based on the presence of an IPSP (Fig. 1D). We found that the spontaneous firing rate of DLS-targeted neurons (24.25 $\pm$ 2.5 Hz; 5 of the 26 cells not spontaneously active) was significantly higher compared to DMS-targeted SNr neurons (17.66 $\pm$ 1. 35 Hz; 3 of the 24 cells not spontaneously active) (Fig. 1E). The input resistance (R_{in}) of DMS-targeted SNr neurons (469.9 $\pm$ 40.9 megohms) was significantly higher than DLS-targeted neurons (278.6 $\pm$ 25.4 megohms) (Fig. 1F), which might indicate higher excitability of DMS-targeted neurons. We found fast rebound firing responses to hyperpolarization in most DMS-targeted and DLS-targeted neurons (Fig. 1G and fig. S1F). However, a significantly higher number of DMS-targeted neurons displayed prolonged rebound firing responses when compared to DLS-targeted neurons (Fig. 1G and fig. S1F). These results indicate that DMS-targeted and DLS-targeted SNr neurons differ in their intrinsic properties and post-inhibitory rebound responses.

We next studied the firing responses of SNr neurons during DMS or DLS terminal stimulation using trains of stimuli delivered at 10 and 20 Hz. We found that 10-Hz stimulation induced partial inhibition of firing at DMS-[M]SNr (light off, 11.2 $\pm$ 1.8 Hz; light on, 6.7 $\pm$ 1.5 Hz) and DLS-[L]SNr inputs (light off, 19.8 $\pm$ 2.7 Hz; light on, 10 $\pm$ 2.5 Hz), whereas a 20-Hz stimulation strongly inhibited firing in both the DMS-[M]SNr input (light off, 10.6 $\pm$ 1.1 Hz; light on, 0.9 $\pm$ 0.6 Hz) and the DLS-[L]SNr input (light off, 15.2 $\pm$ 1.8 Hz; light on, 0.75 $\pm$ 0.72 Hz) (Fig. 1H). Post-inhibitory prolonged rebound responses emerged in most DMS-targeted and a subset of DLS-targeted SNr neurons in response to 10- or 20-Hz stimulation (Fig. 1I). These findings demonstrate that striatal inputs can induce post-inhibitory rebound firing in SNr neurons in a subpopulation-dependent manner.

Differential organization of STN inputs to the medial and lateral SNr

Because of the functional differences of direct pathway striatal inputs on distinct subregions of the SNr, we next sought to determine whether functional differences exist in indirect pathway STN inputs to the [M]SNr and [L]SNr. We virally expressed a Cre-dependent Chronos (AAV5-hSyn-FLEX-Chronos-GFP) in the STN of VGlut2-Cre mice (Fig. 2A). Here, we could not define [M]SNr and [L]SNr neurons based on their striatal input, but we based our classification on their spatial location. To ensure that we were recording from distinct SNr populations, we first confirmed that R_{in} was significantly higher in [M]SNr than [L]SNr neurons (fig. S2A), which matched previous data based on striatal input specificity (Fig. 1A). The amplitude of optically-evoked excitatory post-synaptic currents (oEPSCs) was significantly higher at STN-[L]SNr (0.52 $\pm$ 0.1 nA) over STN-[M]SNr (0.23 $\pm$ 0.05 nA) synapses (Fig. 2B), indicating that STN inputs are biased to the lateral SNr. We then reasoned that STN inputs might be scaled to the different intrinsic properties of SNr subpopulations. We found a significant correlation ($r^2 = 0.5338$) between the amplitude of oEPSCs at STN-SNr synapses and the R_{in} of recorded neurons (Fig. 2C). Using paired stimuli delivered with a 50-ms interpulse interval, we found that the PPR at STN-[M]SNr synapses was facilitating (PPR, 1.3 $\pm$ 0.11), whereas no net facilitation or depression
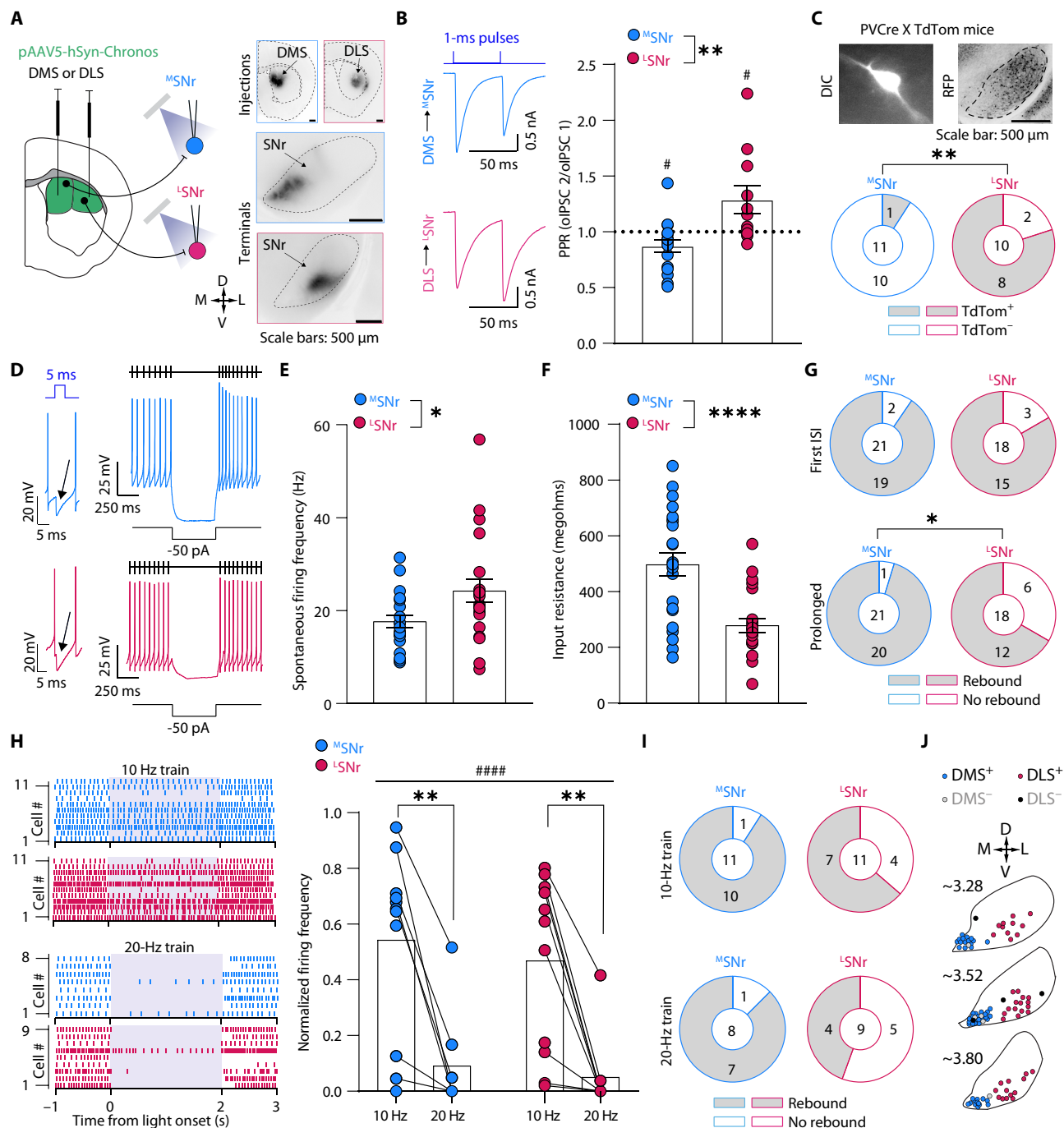
Fig. 1. Input-output organization of DMS-SNr and DLS-SNr projections. (**A**) Left: Viral injection schematic. Right: validation of Chronos-GFP expression in DMS/DLS (injection sites, top) and SNr (terminals, bottom). M, medial; D, dorsal; L, lateral; V, ventral. (**B**) Paired-pulse ratio (PPR) at DMS-^{M}SNr ($n = 17$ cells, 10 slices, 6 mice) and DLS-^{L}SNr synapses ($n = 11$ cells, 10 slices, 5 mice) (one-sample t test, hypothetical value of 1; DMS-^{M}SNr, $P = 0.04$; and DLS-^{L}SNr, $P = 0.045$; Mann-Whitney test, two-tailed, $P = 0.0024$). (**C**) Quantification of PV expressing (TdTom$^+$) and not expressing (TdTom$^-$) neurons among DMS-targeted ($n = 11$ cells, 7 slices, 4 mice) and DLS-targeted SNr cells ($n = 10$ cells, 9 slices, 4 mice) (Fisher's exact test, $P = 0.0019$). (**D**) Example traces and protocols for electrophysiological characterization of DMS-targeted and DLS-targeted SNr neurons. (**E**) Spontaneous firing frequency of DMS-targeted ($n = 21$ cells, 17 slices, 7 mice) and DLS-targeted SNr neurons ($n = 21$ cells, 14 slices, 6 mice) (Mann-Whitney test, two-tailed, $P = 0.043$). (**F**) Input resistance of DMS-targeted ($n = 24$ cells, 17 slices, 6 mice) and DLS-targeted ($n = 22$ cells, 15 slices, 7 mice) SNr neurons (unpaired t test, two-tailed, $P < 0.0001$). (**G**) Proportion of ^{M}SNr and ^{L}SNr neurons displaying fast or prolonged (Fisher's exact test, $P = 0.035$) rebound responses. (**H**) Effects of DMS inputs ($n = 11$ cells, 10 slices, 4 mice) and DLS inputs ($n = 11$ cells, 9 slices, 3 mice) on SNr neuron firing (mixed-effects analysis, frequency main effect, $F_{1,20} = 25.74$, $P < 0.0001$; Šídák's multiple comparisons test; DMS-^{M}SNr, $P = 0.0016$; DLS-^{L}SNr, $P = 0.0024$). (**I**) Proportion of neurons displaying rebound firing following DMS-^{M}SNr and DLS-^{L}SNr input stimulation at 10 or 20 Hz. (**J**) Location of the DMS-targeted and DLS-targeted SNr neurons presented in the figure.
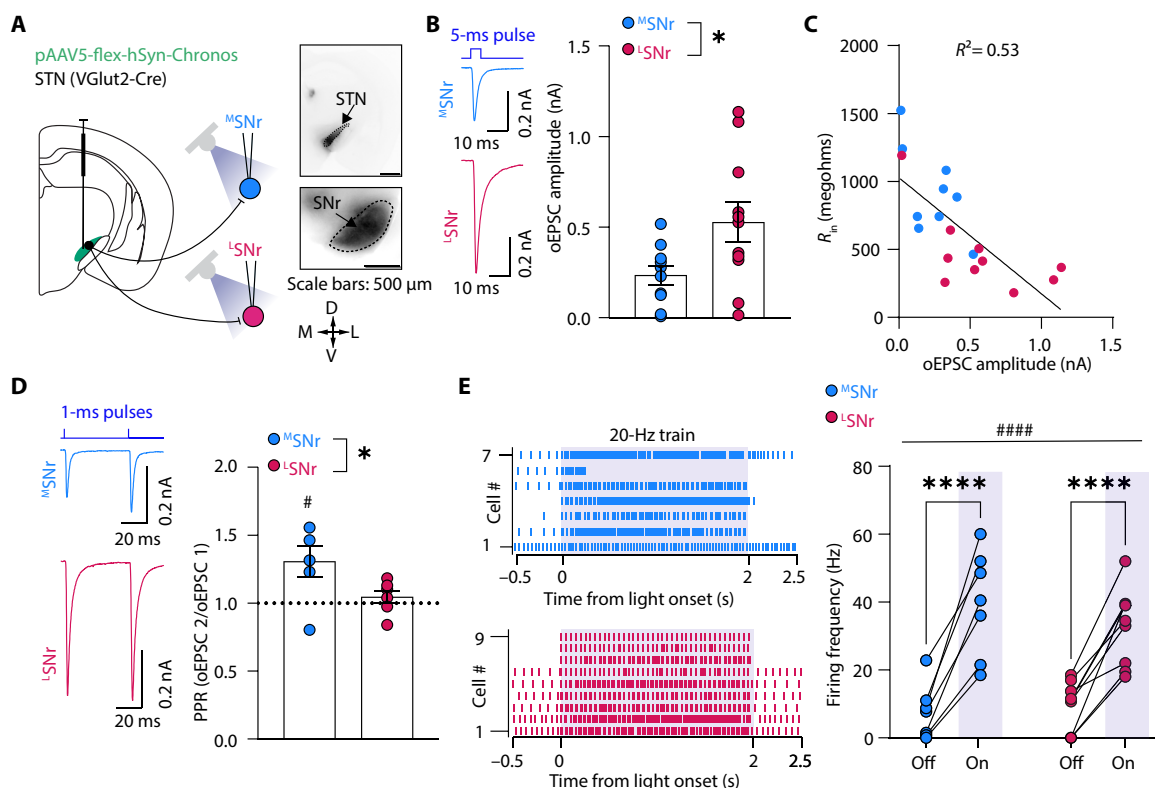
Fig. 2. Differential organization of STN inputs to the medial and lateral SNr. (**A**) Left: Viral injection schematic. Right: Validation of Chronos-GFP expression in STN (injection site, top) and SNr (terminals, bottom). (**B**) Amplitude of oEPSCs at STN-^{M}SNr ($n = 10$ cells, 10 slices, 5 mice) and STN-^{L}SNr ($n = 11$ cells, 10 slices, 6 mice) synapses (unpaired t test, two-tailed, $P = 0.031$). (**C**) Correlation of oEPSC amplitude and R_{in} at STN-SNr synapses ($n = 19$ cells, 14 slices, 6 mice) ($R^2 = 0.53$; $P = 0.0004$). (**D**) PPR at STN-^{M}SNr ($n = 6$ cells, 6 slices, 5 mice) and STN-^{L}SNr synapses ($n = 7$ cells, 6 slices, 4 mice) (one-sample t test, hypothetical value of 1; STN-^{M}SNr, $P = 0.04$; unpaired t test, two-tailed, $P = 0.04$). (**E**) Effects of STN inputs on ^{M}SNr neuron firing ($n = 7$ cells, 7 slices, 4 mice) and ^{L}SNr neuron firing ($n = 9$ cells, 8 slices, 3 mice) [two-way repeated-measures (RM) analysis of variance (ANOVA), main effect of light $F_{1,14} = 109.4$, $P < 0.0001$; Šídák's multiple comparisons test; ^{M}SNr, $P < 0.0001$; ^{L}SNr, $P < 0.0001$].

emerged at STN-^{L}SNr (PPR, 1.04 ± 0.04) inputs, and that PPRs at STN-^{M}SNr and STN-^{L}SNr synapses were significantly different (Fig. 2D). Hence, STN-SNr inputs are biased to the ^{L}SNr also due to higher release probability at STN-^{L}SNr synapses.

We next studied SNr firing responses while stimulating STN inputs using 20-Hz stimulus trains. The increase in firing relative to baseline produced by STN terminal stimulation was similar in ^{M}SNr (light off, 7.5 ± 3 Hz; light on, 39.5 ± 5 Hz) neurons compared to that in ^{L}SNr (light off, 9.2 ± 2.5 Hz; light on, 33 ± 3.7 Hz) neurons (Fig. 2E). Hence, STN inputs have different synaptic strengths in the different SNr subregions but are sufficient to induce firing in ^{M}SNr and ^{L}SNr neurons.

Altered DLS-SNr inputs but not DMS-SNr inputs following chronic alcohol exposure

In our circuit characterization, we established key synaptic differences in DMS, DLS, and STN inputs to the ^{M}SNr and ^{L}SNr, serving as a starting point to examine alcohol effects on distinct SNr subcircuits.

We virally expressed Chronos in the DMS or DLS and subjected 3- to 4-month-old C57BL mice to chronic intermittent alcohol vapor exposure (CIE) and a control group to air exposure (AIR) (Fig. 3A). We performed electrophysiological experiments during extended withdrawal (3 to 21 days after withdrawal), a period

associated with altered action control and cortico-striatal synaptic dysfunctions (*25, 26*) following CIE. We first investigated the presynaptic properties of DMS-SNr and DLS-SNr synapses between AIR and CIE mice. We found that CIE did not induce a change in PPR at DMS-SNr synapses, whereas CIE induced an increase in PPR at DLS-SNr synapses (Fig. 3B). The increased PPR at DLS-SNr synapses might be indicative of a reduced release probability. To investigate whether the PPR changes at DLS-SNr synapses were associated with overall changes in synaptic strength, we recorded asynchronous inhibitory postsynaptic currents (aIPSCs) (Fig. 3C). We found that CIE did not alter the frequency and amplitude of aIPSCs at DMS-SNr synapses (Fig. 3, D and E). Conversely, we found that CIE induced an increase in the amplitude and frequency of aIPSCs at DLS-SNr synapses (Fig. 3, D and E). The increased synaptic strength at DLS-SNr synapses likely reflects a postsynaptic mechanism accompanied by a compensatory presynaptic decrease in release probability. Overall, the net effect of CIE appears to be selective potentiation of DLS-SNr synapses.

Unaltered STN inputs to the SNr following chronic alcohol exposure

A potentiated DLS-SNr synapse might enhance the direct pathway influence over lateral SNr output following CIE. STN inputs to the SNr, particularly those to the lateral SNr, may counteract striatal inputs
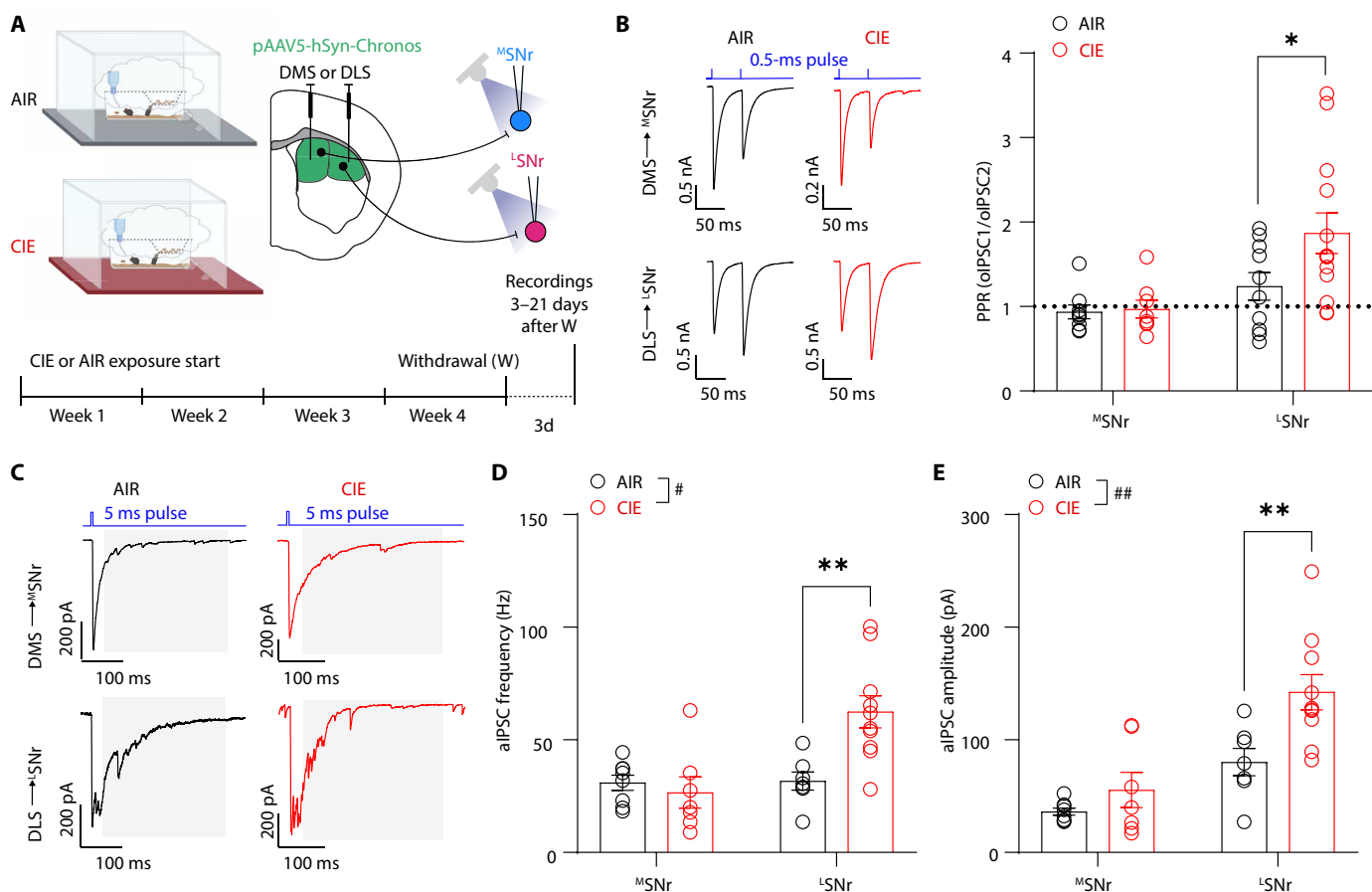
Fig. 3. CIE potentiates DLS-SNr projections. (**A**) Experimental schematic and timeline (created with BioRender.com). (**B**) CIE effects on PPRs at DMS-^{M}SNr (AIR: $n = 9$ cells, 7 slices, 4 mice; CIE: $n = 7$ cells, 7 slices, 5 mice) and DLS-^{L}SNr synapses (AIR: $n = 11$ cells, 7 slices, 4 mice; CIE: $n = 13$ cells, 9 slices, 5 mice) (two-way RM ANOVA, main effect of treatment $F_{1,36} = 3.567$, $P = 0.067$; main effect of synapse, $F_{1,36} = 8.758$, $P = 0.0054$; Šídák's multiple comparisons test ^{L}SNr AIR versus ^{L}SNr CIE, $P = 0.0178$). (**C**) Example traces of asynchronous IPSCs (aIPSCs) recorded at DMS-^{M}SNr and DLS-^{L}SNr synapses in AIR and CIE groups. (**D**) CIE effects on aIPSC frequency at DMS-^{M}SNr (AIR: $n = 8$ cells, 5 slices, 3 mice; CIE: $n = 7$ cells, 4 slices, 3 mice) and DLS-^{L}SNr synapses (AIR: $n = 7$ cells, 4 slices, 3 mice; CIE: $n = 10$ cells, 9 slices, 5 mice) (two-way RM ANOVA, main effect of treatment, $F_{1,28} = 4.87$, $P = 0.0357$; main effect of synapse, $F_{1,28} = 9.3$, $P = 0.005$; interaction treatment × synapse, $F_{1,28} = 8.5$, $P = 0.0067$; Šídák's multiple comparisons test; ^{L}SNr AIR versus ^{L}SNr CIE, $P = 0.0018$). (**E**) CIE effects on aIPSC amplitude (AIR: $n = 8$ cells, 5 slices, 3 mice; CIE: $n = 7$ cells, 4 slices, 3 mice) at DMS-^{M}SNr and DLS-^{L}SNr (AIR: $n = 7$ cells, 4 slices, 3 mice; CIE: $n = 10$ cells, 9 slices, 5 mice) synapses (two-way RM ANOVA, main effect of treatment, $F_{1,28} = 9.254$, $P = 0.0051$; main effect of synapse, $F_{1,28} = 23.97$, $P < 0.0001$; Šídák's multiple comparisons test; ^{L}SNr AIR versus ^{L}SNr CIE, $P = 0.0044$).

to reduce SNr-mediated behavioral outputs (*34*). We therefore sought to investigate whether CIE produced changes in STN inputs to the SNr. VGluT2-Cre mice were injected with a Cre-dependent version of Chronos in the STN and allocated to AIR or CIE groups. Patch-clamp recordings were performed during prolonged withdrawal (3 to 21 days after withdrawal) (Fig. 4A). We found that CIE did not affect the oEP-SC amplitude at STN-^{M}SNr and STN-^{L}SNr synapses (Fig. 4B). Similarly, we found that CIE did not affect the PPR at STN-^{M}SNr and STN-^{L}SNr synapses (Fig. 4C). These results indicate that CIE did not alter STN inputs to the ^{M}SNr and ^{L}SNr. In summary, our synaptic characterization indicates that CIE might facilitate direct pathway control over lateral SNr output via strengthened DLS-SNr inputs.

Increased role for DLS dSPNs in action execution following chronic alcohol exposure

Cognitive/executive and motor impairments in AUD may be protracted during extended withdrawal. To probe whether altered DLS-SNr synapses contribute to altered cognitive/executive and motor

functions following CIE, we trained mice in a random ratio (RR) instrumental procedure while performing targeted chemogenetic silencing of DLS dSPNs. Drd1-Cre$^+$ mice or Cre$^-$ littermates were injected with AAV-DIO-hM4D(Gi)-mCherry in the DLS and randomly allocated to AIR or CIE groups (Fig. 5A). The activation of hM4D(Gi) by clozapine-*N*-oxide (CNO) decreased GABA release at striatonigral inputs (fig. S3C), in agreement with what previously observed in vivo at dSPN-GPe bridge collateral terminals (*35*). Six to 7 days after withdrawal, AIR (Cre$^-$ and Cre$^+$) and CIE (Cre$^-$ and Cre$^+$) mice underwent operant conditioning for 20% sucrose reward that began with training for 5 days of fixed ratio of 1 and then progressed to training for 2 days of RR 10 and 4 days of RR 20 (Fig. 5B). Mice received CNO (5 mg/kg) injections during RR training to inhibit dSPNs in the DLS. Three-way analysis of variance (ANOVA) analysis (factors: time, treatment, and genotype) revealed a significant interaction between session, genotype, and treatment in the lever press number (fig. S3A), whereas this interaction was trending for the lever press frequency (fig. S3B). This analysis
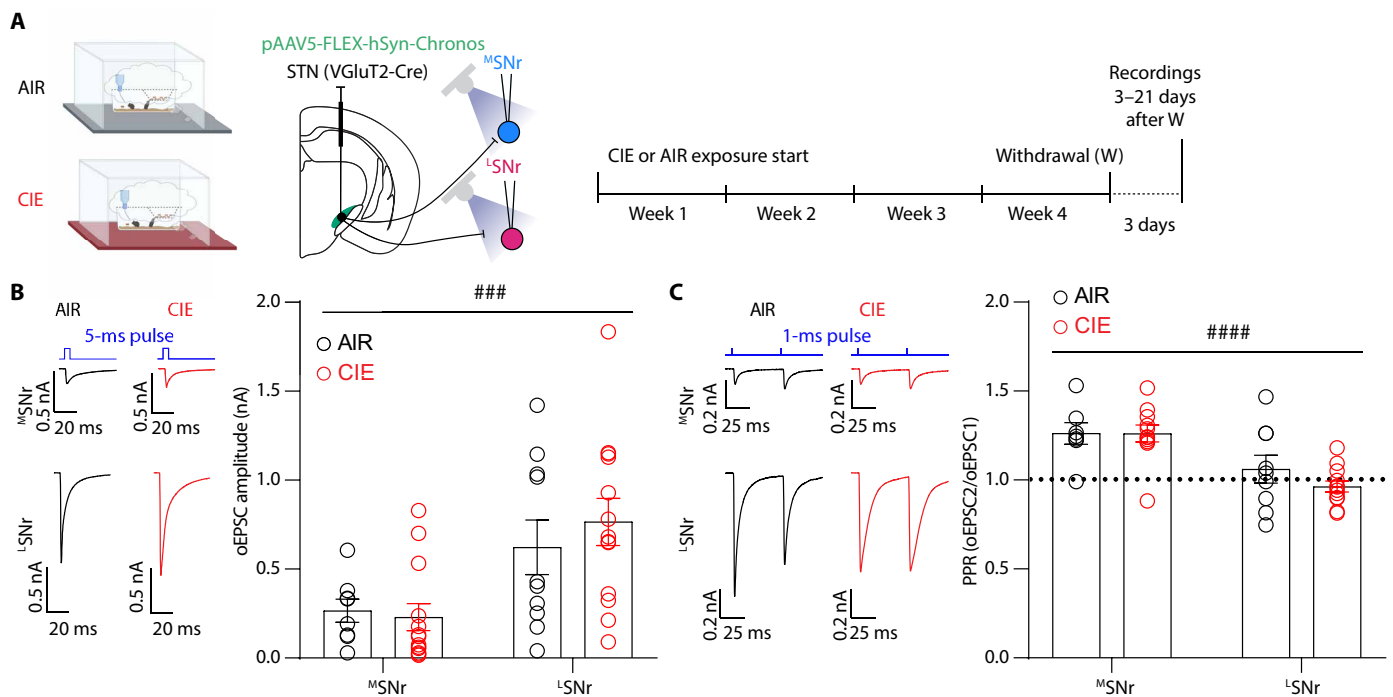
Fig. 4. CIE does not affect STN-SNr inputs. (**A**) Experimental schematic for viral injections and timeline of AIR or CIE exposure and electrophysiological recordings (created with BioRender.com). (**B**) CIE effects on the amplitude of oEPSCs at STN-^{M}SNr (AIR: $n = 8$ cells, 8 slices, 3 mice; CIE: $n = 13$ cells, 13 slices, 4 mice) and STN-^{L}SNr (AIR: $n = 10$ cells, 10 slices, 4 mice; CIE: $n = 13$ cells, 13 slices, 5 mice) synapses (two-way ANOVA, main effect of location, $F_{1,40} = 14.01$, $P = 0.0006$). (**C**) CIE effects on PPRs at STN-^{M}SNr (AIR: $n = 7$ cells, 7 slices, 3 mice; CIE: $n = 11$ cells, 11 slices, 4 mice) and STN-^{L}SNr (AIR: $n = 9$ cells, 9 slices, 3 mice; CIE: $n = 12$ cells, 12 slices, 5 mice) synapses (two-way ANOVA, main effect of location, $F_{1,35} = 21.2$, $P < 0.0001$).

revealed that chemogenetic inhibition differentially affects AIR and CIE mice depending on the session. The lack of a main effect of alcohol indicated that alcohol exposure per se was not sufficient to alter behavioral performance.

In AIR mice, chemogenetic inhibition of DLS-dSPNs did not affect the behavioral performance measured as number of lever presses (Fig. 5C), frequency of lever presses (Fig. 5D), head entries (Fig. 5E), and reinforcers earned (Fig. 5F). These results indicate that the function of DLS dSPNs was not necessary to sustain action execution in AIR mice.

In CIE mice, chemogenetic inhibition of DLS-dSPNs significantly reduced the total number of lever presses (Fig. 5G), the lever pressing frequency (Fig. 5H), and the number of reinforcers earned (Fig. 5J), whereas the number of head entries remained unchanged (Fig. 5I). This analysis indicated that hM4D(Gi)-expressing ^{CIE}Cre$^+$ mice showed fewer and slower lever presses and fewer rewards earned during CNO treatment than ^{CIE}Cre$^-$ mice. These results indicate that the function of DLS dSPNs becomes necessary for action execution in CIE mice. Overall, our findings indicate that strengthened DLS-SNr synapses contribute to an abnormal functional control of action execution following chronic alcohol exposure.

DISCUSSION
Here, we describe a distinctive functional organization of striatal and subthalamic synaptic inputs to the medial and lateral SNr and investigate alcohol effects on distinct SNr subcircuits. We found that chronic inhalational alcohol exposure potentiated the inputs from the dorsolateral striatum to the SNr, likely contributing to a circuit shift in the control of action execution by the BG.

Synaptic inputs to the medial and lateral SNr are differentially organized
Subpopulations of the SNr have been previously classified on the basis of their source of striatal input, output connectivity, and molecular identity. We found that DLS dSPNs primarily synapse onto PV$^+$ SNr neurons, whereas the DMS dSPNs primarily innervate non–parvalbumin-expressing (PV$^-$) SNr neurons. Previous studies indicate that the second largest subpopulation of SNr neurons consists of GAD2$^+$/VGAT$^+$/PV$^-$ neurons (*13*) or GAD2$^+$ neurons (*21*), and future studies will address whether DMS-targeted SNr neurons fall within this category. Our results agree with an enrichment of PV$^+$ neurons in the ventrolateral SNr (*21*, *24*) and with higher R_{in} and lower baseline firing rate in PV$^-$ over PV$^+$ SNr neurons (*24*). Furthermore, our findings support a gradient of intrinsic neuronal properties along the mediolateral axis of the SNr (*13*).

Within the SNr, PV$^+$ and PV$^-$ subpopulations have been found to control distinct aspects of motor performance (*23*) and sleep states (*21*). Therefore, the DMS and DLS inputs have the potential to control distinct SNr-dependent behavioral outputs by targeting molecularly distinct SNr neurons.

We observed specialized synaptic properties of parallel striatal inputs to the SNr, namely, short-term facilitation at DLS-SNr synapses and short-term depression at DMS-SNr synapses. Previous reports using electrical or optogenetic stimulation found that short-term facilitation is characteristic of striatonigral synapses (*36*, *37*).
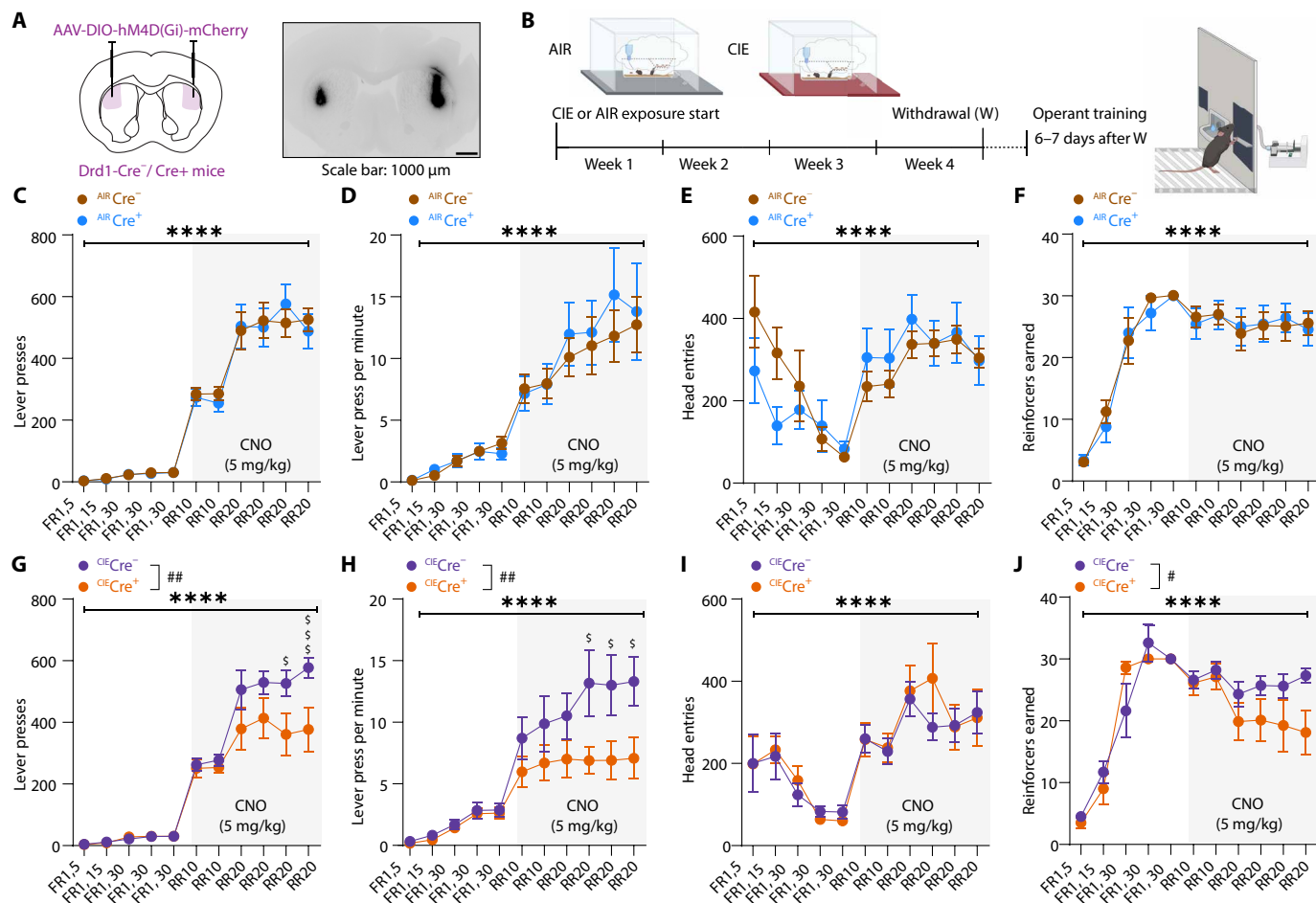
Fig. 5. CIE enhances the contribution of DLS dSPNs in action execution. (**A**) Validation of AAV-DIO-hM4D(Gi)-mCherry expression in the DLS. (**B**) Experimental timeline (created with BioRender.com). N numbers (mice): [AIR]Cre⁻ (12), [AIR]Cre⁺ (9), [CIE]Cre⁻ (10), and [CIE]Cre⁺ (8). (**C**) Lever presses in mice (two-way RM ANOVA, main effect of session, $F_{10,190} = 120.4$, $P < 0.0001$). (**D**) Lever presses per minute in [AIR]Cre⁻ and [AIR]Cre⁺ mice (two-way RM ANOVA, main effect of session, $F_{10,190} = 28.43$, $P < 0.0001$). (**E**) Head entries in [AIR]Cre⁻ and [AIR]Cre⁺ mice (mixed-effect analysis, main effect of session, $F_{10,189} = 8.602$, $P < 0.0001$). (**F**) Reinforcers earned in [AIR]Cre⁻ and [AIR]Cre⁺ mice (two-way RM ANOVA, main effect of session, $F_{10,190} = 42.76$, $P < 0.0001$). (**G**) Lever presses in [CIE]Cre⁻ and [CIE]Cre⁺ mice (two-way RM ANOVA, main effect of session, $F_{10,160} = 87.82$, $P < 0.0001$; main effect of genotype, $F_{10,16} = 4.88$, $P = 0.0421$; interaction session × genotype, $F_{10,160} = 3.08$, $P = 0.0013$; Šídák's multiple comparisons test; RR20-3, $P = 0.0122$; RR20-4, $P = 0.0009$). (**H**) Lever presses per minute in [CIE]Cre⁻ and [CIE]Cre⁺ mice (two-way RM ANOVA, main effect of session, $F_{10,160} = 24.8$, $P < 0.0001$; main effect of genotype, $F_{10,16} = 3.672$, $P = 0.0734$; interaction session × genotype, $F_{10,160} = 2.518$, $P = 0.0077$; Šídák's multiple comparisons test; RR20-2, $P = 0.0333$; RR20-3, $P = 0.0433$; RR20-4, $P = 0.0359$). (**I**) Head entries in [CIE]Cre⁻ and [CIE]Cre⁺ mice (two-way RM ANOVA, main effect of session, $F_{10,160} = 11.54$, $P < 0.0001$). (**J**) Reinforcers earned in [CIE]Cre⁻ and [CIE]Cre⁺ mice (two-way RM ANOVA, main effect of session, $F_{10,160} = 31.54$, $P < 0.0001$; interaction session × genotype, $F_{1,16} = 2.087$, $P = 0.0283$).

These distinct synaptic properties may emerge in response to distinct functional demands of postsynaptic SNr neurons and may result from the distinct gene expression profiles of dSPNs located in the DMS and DLS, especially in those genes related to synaptic function (*38*). These subcircuit-specific properties may generalize to other striatonigral projections, including the one the ventrolateral striatum (*12*, *16*).

Synaptic facilitation may be required at DLS-SNr synapses to sustain postsynaptic responses in SNr neurons with lower excitability. In contrast, synaptic depression at DMS-SNr synapses may contribute to faster responses in the highly excitable DMS-targeted SNr neurons. Here, we find that DMS- and DLS-targeted subpopulations of SNr neurons differ in their rebound firing capability, with a higher number of DMS-targeted neurons displaying prolonged rebound responses. We demonstrate that striatal inputs can elicit rebound

responses in the majority of DMS-targeted and a subpopulation of DLS-targeted SNr neurons. Overall, we propose that the interplay between specialized synaptic input properties and neuronal intrinsic properties contributes to fine-tune signal processing in parallel SNr subcircuits (*13*, *21*).

We find that STN synaptic inputs are stronger in the lateral compared to medial SNr and scale with the R_{in} of SNr neurons. This organization allowed STN inputs to sustain firing responses throughout SNr subregions. Yet, a postsynaptic scaling of glutamatergic synapses alone was not sufficient to explain our findings, as we observed higher presynaptic release probability on STN inputs to the lateral over the medial SNr. These different presynaptic properties may be explained as a function of molecular differences in STN subpopulations targeting the medial and lateral SNr (*39*) or result from distinct presynaptic modulation of these inputs.

Our findings indicate a subcircuit-specific synaptic organization in the SNr that might generalize to other synaptic inputs, including the pallidonigral projection. We speculate that a consequence of this differential organization might be a differential vulnerability of distinct synaptic inputs to the SNr in pathological conditions affecting BG functioning, including AUD and Parkinson's disease (26, 40, 41).

Potentiated DLS-SNr inputs are accompanied by altered BG control of action execution following chronic alcohol exposure

Our study indicates a selective alteration of DLS-SNr but not DMS-SNr inputs following chronic alcohol exposure. In light of previous literature indicating alcohol-induced increased excitability and in vivo calcium activity of DMS dSPNs and altered thalamic and cortical inputs to DMS dSPNs (30, 31, 42–44), we cannot exclude that different alcohol exposure paradigms might also induce DMS-SNr synaptic input alterations. We found that chronic alcohol exposure significantly increased the PPR at DLS-SNr inputs, indicating decreased presynaptic probability of GABA release following chronic alcohol exposure. Moreover, we found increased frequency and amplitude of aIPSCs at DLS-SNr synapses, indicating an increased strength of DLS-SNr inputs. Our findings imply the presence of a postsynaptic mechanism that potentiates DLS-SNr inputs via an increased number of GABAergic synapses, an increased availability of GABA type A (GABA_A) receptors, or changes in channel conductance due to modifications in their subunit composition (3, 4). In parallel, compensatory presynaptic changes might explain the increase in PPR at DLS-SNr inputs, including altered G protein–coupled receptor signaling.

The changes that we observed at DLS-SNr inputs may be linked to previous evidence supporting alcohol-induced DLS disinhibition. These include decreased GABAergic synaptic transmission onto SPNs in DLS in a mouse model of binge drinking (45). Similarly, chronic alcohol drinking was found to reduce GABAergic synaptic inputs, potentiate glutamatergic inputs, and increase the excitability of SPNs in the putamen of macaque monkeys (46, 47). We previously reported that chronic intermittent ethanol vapor exposure promotes dendritic arborization of DLS SPNs and disinhibition of cortico-striatal inputs via reduced endocannabinoid-dependent plasticity (48). These changes were found to increase the function of DLS neurons in the performance of an in vivo visual discrimination task (48). In mice, potentiated anterior insular cortex inputs to the DLS via impaired μ-opioid–dependent long-term depression (49) were implicated in maintaining alcohol binge drinking in male mice (50). These synaptic changes may drive cellular adaptations in DLS dSPNs affecting their efferent projections to the SNr.

Here, we find that potentiated DLS-SNr but unaltered STN-SNr inputs might contribute to enhancement of the striatal GABAergic drive on lateral SNr neuron output in CIE mice. Both CIE and AIR mice were similarly capable of executing lever pressing actions under an RR schedule, but the performance was selectively impaired in CIE mice when DLS dSPNs were inhibited with DREADDs. The impaired lever-pressing execution induced by chemogenetic inhibition of DLS dSPNs in CIE mice cannot be explained simply as a generalized reduction in motor output, because this manipulation did not similarly impair head entries. In RR training, DLS dSPNs were found to progressively disengage throughout training in healthy mice (51). One possible explanation for our results is that, in CIE mice, DLS dSPNs fail to disengage and assume a crucial role in action execution during high ratio requirements. An alternative explanation might entail a motivational component, where, in CIE but not AIR control mice, DLS dSPNs are necessary to sustain the increasing effort imposed by a higher ratio schedule.

Overall, we find that GABAergic and glutamatergic synaptic inputs differ in their properties between the neuronal subpopulations of the medial and lateral SNr and that striatal inputs to the lateral SNr are selectively affected by chronic ethanol exposure. These findings have implications for behavioral flexibility in AUD, as an abnormal engagement of the sensorimotor BG circuit during action learning and execution might interfere with associative circuits in the acquisition of novel goal-directed actions.

MATERIALS AND METHODS
Ethical approval
Experiments were conducted in accordance with the National Institutes of Health's *Guide for the Care and Use of Laboratory Animals*, and all experimental procedures were approved by the National Institute on Alcohol Abuse and Alcoholism Animal Care and Use Committee (protocol no. LIN-DL-1). Mice were housed in groups of two to four in the NIAAA vivarium on a 12-hour light cycle with ad libitum access to food and water.

Animals
VGluT2-IRES-Cre mice [B6J.129S6(FVB)-Slc17a6tm2(cre)Lowl/MwarJ, cat. no. JAX 028863], PV-IRES-Cre mice [B6.129P2-Pvalbtm1(cre)Arbr/J, cat. no. JAX 017320], Td-Tomato mice [B6-Cg-Gt(ROSA)26Sortm14(CAGtdTomato)Hze/J, cat. no. 007914], and C57BL-6J mice were purchased from the Jackson laboratory (JAX; Bar Harbor, ME, USA). Heterozygous Drd1-Cre [STOCK Tg(Drd1-cre)FK150Gsat/Mmucd] mice were purchased from Gensat and crossed with C57BL-6J mice. VGluT2-IRES Cre and PV-IRES-Cre homozygous and heterozygous (het) male or female mice were crossed with C57BL-6J. Homozygous PV-IRES-Cre mice were crossed with homozygous Td-Tomato mice to generate PVCre-TdTom mice. Experiments were conducted on male and female mice aged >3 months. All mice involved in the CIE experiments initiated the CIE exposure between 3 and 4 months of age. Hence, mice were tested for behavior or slice electrophysiology between 4 and 5 months of age. Genotyping was performed by polymerase chain reaction on genomic DNA from ear biopsies.

Surgical procedures
Deep anesthesia was performed in an induction chamber using 5% isoflurane. Animals were quickly transferred to a stereotaxic frame that delivered isoflurane at 1 to 3% through the mouthpiece for the whole duration of the surgery. A Hamilton syringe preloaded with the viral solution was inserted in the brain parenchyma to target the DLS [antero-posterior (AP), +0.9; medio-lateral (ML), ±2.4; dorso-ventral (DV), −3.2], DMS (AP, +0.9; ML, ±1.4; DV, −3.2), or STN (AP, −1.9; ML, ±1.7; DV, −4.5). pAAV5-Syn-Chronos-GFP (200 nl; Addgene, plasmid no. 59170, 5×10^{12} viral genomes (vg)/ml) were injected in the DMS or DLS (injection rate, 25 nl/min) of C57BL-6J mice. AAV5-hSyn-FLEX-Chronos-GFP (300 nl; University of North Carolina at Chapel Hill viral core, 7×10^{12} vg/ml) was injected in the STN (injection rate, 50 nl/min) of VGlut2-IRES-Cre mice. AAV2-hSyn-DIO-HM4D(Gi)-mCherry (300 nl; Addgene, plasmid no. 50475, 7×10^{12} vg/ml) was injected in the DLS of Drd1-Cre[+] mice

and their Cre⁻ littermates. For validation of DREADD effects on DS-SNr synapses, 400 nl of pAAV5-Syn-Chronos-GFP and AAV2-hSyn-DIO-HM4D(Gi)-mCherry were co-injected in the striatum of Drd1-Cre⁺ mice (AP, 0.9; ML, ±2; DV, −3.2). Following the injection of the viral solution, the syringe was kept in place for 5 min and then retracted. The wounded skin was closed using skin glue (Vetbond, 3M). Postoperative care included the administration of ketoprofen (5 mg/kg, subcutaneously) following surgeries and 2 days of recovery, where half of the cage was placed on a heated pad.

Brain slice preparation for patch-clamp experiments and validation of viral expression

Mice were deeply anesthetized with isoflurane and decapitated. The brain was collected and transferred to a slicing chamber filled with ice-cold sucrose-based cutting solution containing the following: 194 mM sucrose, 30 mM NaCl, 4.5 mM KCl, 26 mM $NaHCO_3$, 1.2 mM NaH_2PO_4, 10 mM D-glucose, and 1 mM $MgCl_2$, saturated with 95% O_2/5% CO_2. Coronal sections (250 μm) containing the SNr, STN, or striatum were obtained using a Leica VT1200S Vibratome (Leica Microsystems, Buffalo Grove, IL) and transferred to an incubation chamber filled with artificial cerebrospinal fluid (aCSF) containing: 124 mM NaCl, 4.5 mM KCl, 26 mM $NaHCO_3$, 1.2 mM NaH_2PO_4, 10 mM D-glucose, 1 mM $MgCl_2$, and 2 mM $CaCl_2$, saturated with 95% O_2/5% CO_2). Slices were incubated for 45 to 60 min at 32°C and then maintained at room temperature. Slices containing the STN, SNr, or striatum were transferred to an aCSF-filled petri dish, and low-magnification epifluorescence images were acquired using a Zeiss Axiozoom microscope (Carl Zeiss, Oberkochen, Germany) via a Zeiss Axiocam MR monochrome charge-coupled device (CCD) camera for validation of viral expression.

Whole-cell patch-clamp recordings and analysis

Hemislices were transferred to a recording chamber perfused with aCSF at 30° to 32°C. Neurons were visualized with an upright microscope (Model BX51WI, Olympus, Waltham, MA) using a 10× air objective or 40× water objective (LUMPlanFL, 0.80 numerical aperture) and connected to a CCD camera (SciCam Pro, Scientifica) controlled via the Ocular Imaging acquisition software (Teledyne Photometrics, Tucson, Arizona). Images were obtained using the 10× objective to track the approximate location of the recorded neurons. Recordings from SNr neurons were obtained using micropipettes (2 to 4 megohms) made from 1.5-mm–outer diameter/1.12-mm–inside diameter borosilicate glass with a filament (World Precision Instruments, Sarasota, FL) pulled with a P-97 puller (Sutter Instruments, Novato, CA). The intracellular solution for voltage-clamp recordings of inhibitory postsynaptic currents (IPSCs) contained the following: 150 mM CsCl, 10 mM Hepes, 2.0 mM $MgCl_2$, 0.3 mM Na–guanosine 5′-triphosphate (GTP), 3.0 mM Mg–adenosine 5′-triphosphate (ATP), 0.2 mM 1,2-bis(2-aminophenoxy)ethane-$N,N,N′,N′$-tetraacetic acid–4Cs, and 5.0 mM QX-314. The intracellular solution for voltage-clamp recordings of excitatory post-synaptic currents (EPSCs) contained the following: 114 mM $CsMeSO_3$, 5.0 mM NaCl, 1.0 mM TEA-Cl, 10 mM Hepes, 5.0 mM QX-314, 1.1 mM EGTA, 0.3 mM Na-GTP, and 4.0 mM Mg-ATP. The intracellular solution for current-clamp recordings contained the following: 140 mM mM K-Glu, 10 mM Hepes, 0.1 mM $CaCl_2$, 2 mM $MgCl_2$, 1 mM EGTA, 2 mM ATP-Mg, and 0.2 mM GTP-Na. Voltage-clamp recordings were performed using Multiclamp 700B and a Digidata 1550B digitizer using a low-pass filter of 2 kHz and a sampling frequency of 10 kHz. Current-clamp recordings were performed using Multiclamp 700B and a Digidata 1550B digitizer using a low-pass filter of 2 to 10 kHz and a sampling frequency of 10 kHz. Data were acquired and analyzed using pClamp 10.3 or pClamp 10.6 software (Molecular Devices, Sunnyvale, CA). To isolate IPSCs, the AMPA receptor antagonist 6,7-Dinitroquinoxaline-2,3-dione (DNQX) (10 μM) and the N-methyl-D-aspartate receptor antagonist DL-AP5 (50 μM) were continuously bath applied. To isolate EPSCs, the $GABA_A$ antagonist Gabazine (10 μM) was continuously bath-applied. To record aIPSCs, a modified aCSF was used, whereby Ca^{2+} was replaced by Sr^{2+} (4 mM).

SNr neurons were characterized in voltage-clamp experiments (holding voltage, −50 mV) for their location, appearance, and firing frequency assessed in tight-seal (resistance, >500 megohms) cell-attached mode before the break-in, and absence of a hyperpolarization-activated current (I_h) measured using a −50-mV step in voltage-clamp mode after break-in (*37*). In experiments conducted in PVCre-TdTom mice, the following procedure was followed: Neurons were visualized using differential interference contrast and a tight seal was established; next, yellow light (509 to 551 nm) was briefly delivered via field illumination through the microscope objective (generated via an X-Cite LED driver, Lumen dynamics, and filtered through a Cy3 filter) to label neurons as TdTom⁺ or TdTom⁻; following breakthrough, connectivity was assessed; the field of view of the slice was then changed to reduce sampling bias in the next recording attempt.

oIPSC and oEPSC amplitudes, latency to peak, PPRs, and input resistance in voltage-clamp experiments (measured from the steady state of a −50-mV step) were analyzed using clampfit (pClamp suite). Input resistance in current clamp experiments (measured from the steady state of a −50-pA, 500-ms current step) was analyzed using Easy Electrophysiology (Easy Electrophysiology Ltd., London, England). aIPSC frequency and amplitude were analyzed using Easy Electrophysiology. A minimum of six trials were averaged to calculate oIPSC amplitudes, PPRs, aIPSC amplitude and frequency, and input effects on SNr neuron firing. For rebound firing analysis, a baseline was defined for each cell as the average firing frequency recorded 1 s before a −50-pA, 500-ms current step or before optogenetic stimulation of striatal inputs. Rebound responses were then analyzed by normalizing to baseline the first instantaneous frequency (fast rebound) or the average firing frequency of 400 ms (prolonged rebound) following negative current injections or 1 s following optogenetic stimulation of striatal inputs. Neurons in which firing increased by more than 5% from to baseline were defined as "rebounders."

Optogenetic stimulation protocols for patch-clamp recordings

The light was generated via an X-Cite LED driver (Lumen dynamics), delivered via field illumination through the microscope objective, and filtered through a single band filter to produce ~470-nm illumination. To measure absolute amplitudes of oIPSCs and oEPSCs and evoked aIPSCs, blue light pulses of 5 ms and an optical power of ~10 mW were used. To measure PPRs, the following pulse width was used: Fig. 1B, 0.5 to 2 ms; Fig. 2D, 1 to 5 ms; and Fig. 3B, 0.5 ms; Fig. 4C, 1 ms (the optical power and pulse width were adjusted to the minimum required to produce a stable response; range, 0.56 to

6 mW). For current-clamp experiments, 2-s-long trains of stimuli at 10 or 20 Hz were delivered, using a pulse width of 1 to 5 ms and optical power of ~5 mW. For all experiments, light pulses were delivered every 20 to 30 s.

Procedure for chronic intermittent ethanol exposure

Ethanol vapor exposure was conducted in Plexiglas chambers (Plas Labs Inc., Lansing, MI). A subset of chambers was used to expose mice to vaporized ethanol (CIE group), and a separate subset was used to expose mice to air (AIR group). The chambers were connected to a vaporizer. In the ethanol chamber, 95% ethanol was vaporized through air flow at a rate of 1.5 to 3 liters/min. Vaporized ethanol was combined with another air stream to produce a total flow rate of ~10 liters/min in each chamber. A similar rate of delivery was provided in the air chamber. The rate was adjusted throughout the cycle to produce vapor ethanol concentrations of 0.160 to 0.240 mg/liter. Vapor ethanol concentrations were assessed using a breath analyzer. Mice were exposed to four cycles of CIE, each consisting of four consecutive days in which mice were exposed to 16 hours of ethanol vapor (CIE group) or air (AIR group) followed by 8 hours of withdrawal. In between cycles, mice underwent 72 hours of withdrawal. Mice were not given any loading dose of ethanol or pyrazole injections before the exposure. This procedure yielded average blood ethanol levels of 165.2 ± 10.6 mg/dl. Throughout the 4 weeks of CIE exposure, mice remained in the room containing the vapor chambers. This room had the same light cycle, temperature, and humidity settings as the colony room where mice were previously housed and where mice returned following CIE.

Procedure for blood ethanol concentration measurements

Blood was collected maximum twice from each mouse throughout the 4 weeks of CIE, with a typical interval of 2 weeks between collections. The collection was done through a caudal vein tail nick. Blood (<20 µl) was collected from the tail vein in heparinized hematocrit tubes (Fisherbrand, cat. no. 22-362-566) and rapidly transferred for centrifugation at 10,000 rpm for 5 to 10 min. The serum was isolated, transferred to Eppendorf tubes, and diluted for further processing. Blood ethanol concentration was measured using a colorimetric assay (Pointe Scientific, MI, USA).

Operant conditioning

Forty-eight hours following the end of the fourth CIE cycle, mice underwent food restriction to reach ~90% of their body weight. Operant training started 6 to 7 days following the end of the fourth CIE cycle. Mice received injections of saline or CNO (5 mg/kg) 1 hour before the start of each operant conditioning session. Mice were trained to lever press for 20% sucrose in operant boxes (Med-Associates). Training began with 1 day of magazine training in which no lever was presented, but sucrose was delivered at random intervals (average, 60 s) in the magazine. All mice successfully learned to identify the magazine and consume the reward and were moved to the operant training, which started the following day. During initial training, mice were trained to lever press under a fixed ratio (FR1) schedule (1 lever press = 1 reward) for 5 days, with a time criterion of 60 min, after which the session was interrupted (day 2: FR1, 5 rewards; day 3: FR1, 15 rewards; days 4 to 6: FR1, 30 rewards). Mice were then moved to an RR schedule in which they received a reward after an average of 10 lever presses (RR10, days 7 to 8) and then after an average of 20 lever presses (RR20, days 9 to 12), for a maximum of 30 rewards over 60 min.

Immunohistochemistry and confocal imaging

Mice were anesthetized with pentobarbital (50 mg/kg) before transcardial perfusion with 1× phosphate-buffered saline (PBS), followed by 4% formaldehyde (FA) (4% paraformaldehyde in 1× PBS). Brains were kept in 4% FA overnight and then transferred to 1× PBS until slicing. Free-floating sections (50 µm) were cut using a Pelco easySlicer Vibratome (Ted Pella Inc., Redding, CA, USA). Slices were washed three times for 5 min in 1× PBS and then incubated in a blocking solution containing 5% normal goat serum in PBS-T (0.2% Triton X-100). Slices were then incubated over two nights in 1× PBS containing the primary antibody (rabbit anti–red fluorescent protein; Rockland, cat. no. 600-401-379). Slices were then washed three times for 5 min in 1× PBS and incubated in 1× PBS containing the secondary antibodies for 2 hours (Alexa Fluor 594 goat anti-rabbit; Invitrogen, A11012; 1:500). A final wash of three times for 5 min was performed before mounting using 4′,6-diamidino-2-phenylindole Fluoromount-G (SouthernBiotech, cat no. 0100-20). Low-magnification epifluorescence images were obtained through a Zeiss Axiozoom microscope (Carl Zeiss, Oberkochen, Germany) equipped with standard Cy3 filters via a Zeiss Axiocam MR monochrome CCD camera.

Viruses and reagents

Viruses were aliquoted in 2.5 to 5 µl of aliquots and stored at −80 until use. All drugs (DNQX, DL-AP5, Gabazine, and CNO) were purchased from Tocris.

Statistical analysis

Statistical analysis was performed in GraphPad Prism (GraphPad Software, La Jolla, California), and data were preprocessed in Excel. A ROUT test ($Q = 0.1\%$) was used to identify statistical outliers, and, on the basis of this criterion, we excluded one neuron from the analysis in Fig. 1E. Data were analyzed using two-way repeated-measures ANOVA, mixed-effects analysis with no correction, three-way ANOVA, unpaired t tests, or Mann-Whitney tests. Post-hoc comparisons were analyzed using the Šidák post-hoc test where appropriate. The statistical test used and the significance are indicated in the figures and figure legends. The Shapiro-Wilk test was used to determine whether data were normally distributed. Significance was set at $P < 0.05$ in all analyses and indicated in figures (*, #, and $ for $P < 0.05$; **, ##, and $$ for $P < 0.01$; ***, ###, and $$$ for $P < 0.001$; ****, ####, and $$$$ for $P < 0.0001$). All data are reported as means + SEM.

Supplementary Materials

This PDF file includes:
Figs. S1 to S3

Other Supplementary Material for this manuscript includes the following:
Data file S1

REFERENCES AND NOTES

1. American Psychiatric Association, *Diagnostic and Statistical Manual for Mental Disorders* (American Psychiatric Publishing, ed. 5, 2013).
2. A. F. Carvalho, M. Heilig, A. Perez, C. Probst, J. Rehm, Alcohol use disorders. *Lancet* **394**, 781–792 (2019).

3. K. P. Abrahao, A. G. Salinas, D. M. Lovinger, Alcohol and the brain: Neuronal molecular targets, synapses, and circuits. *Neuron* **96**, 1223–1238 (2017).

4. D. M. Lovinger, M. Roberto, Synaptic effects induced by alcohol. *Curr. Top. Behav. Neurosci.* **13**, 31–86 (2013).

5. G. Egervari, C. A. Siciliano, E. L. Whiteley, D. Ron, Alcohol and the brain: From genes to circuits. *Trends Neurosci.* **44**, 1004–1015 (2021).

6. H. H. Yin, B. J. Knowlton, The role of the basal ganglia in habit formation. *Nat. Rev. Neurosci.* **7**, 464–476 (2006).

7. J. T. Dudman, J. W. Krakauer, The basal ganglia: From motor commands to the control of vigor. *Curr. Opin. Neurobiol.* **37**, 158–166 (2016).

8. S. Arber, R. M. Costa, Networking brainstem and basal ganglia circuits for movement. *Nat. Rev. Neurosci.* **23**, 342–360 (2022).

9. S. Grillner, B. Robertson, The basal ganglia over 500 million years. *Curr. Biol.* **26**, R1088–R1100 (2016).

10. G. F. Koob, N. D. Volkow, Neurocircuitry of addiction. *Neuropsychopharmacology* **35**, 217–238 (2010).

11. J. M. Deniau, P. Mailly, N. Maurice, S. Charpier, The pars reticulata of the substantia nigra: A window to basal ganglia output. *Prog. Brain Res.* **160**, 151–172 (2007).

12. J. Lee, W. Wang, B. L. Sabatini, Anatomically segregated basal ganglia pathways allow parallel behavioral modulation. *Nat. Neurosci.* **23**, 1388–1398 (2020).

13. L. E. McElvain, Y. Chen, J. D. Moore, G. S. Brigidi, B. L. Bloodgood, B. K. Lim, R. M. Costa, D. Kleinfeld, Specific populations of basal ganglia output neurons target distinct brain stem areas while collateralizing throughout the diencephalon. *Neuron* **109**, 1721–1738.e4 (2021).

14. O. Hikosaka, GABAergic output of the basal ganglia. *Prog. Brain Res.* **160**, 209–226 (2007).

15. G. E. Alexander, M. R. DeLong, P. L. Strick, Parallel organization of functionally segregated circuits linking basal ganglia and cortex. *Annu. Rev. Neurosci.* **9**, 357–381 (1986).

16. N. N. Foster, J. Barry, L. Korobkova, L. Garcia, L. Gao, M. Becerra, Y. Sherafat, B. Peng, X. Li, J.-H. Choi, L. Gou, B. Zingg, S. Azam, D. Lo, N. Khanjani, B. Zhang, J. Stanis, I. Bowman, K. Cotter, C. Cao, S. Yamashita, A. Tugangui, A. Li, T. Jiang, X. Jia, Z. Feng, S. Aquino, H.-S. Mun, M. Zhu, A. Santarelli, N. L. Benavidez, M. Song, G. Dan, M. Fayzullina, S. Ustrell, T. Boesen, D. L. Johnson, H. Xu, M. S. Bienkowski, X. W. Yang, H. Gong, M. S. Levine, I. Wickersham, Q. Luo, J. D. Hahn, B. K. Lim, L. I. Zhang, C. Cepeda, H. Hintiryan, H.-W. Dong, The mouse cortico-basal ganglia-thalamic network. *Nature* **598**, 188–194 (2021).

17. P. Redgrave, M. Rodriguez, Y. Smith, M. C. Rodriguez-Oroz, S. Lehericy, H. Bergman, Y. Agid, M. R. DeLong, J. A. Obeso, Goal-directed and habitual control in the basal ganglia: Implications for Parkinson's disease. *Nat. Rev. Neurosci.* **11**, 760–772 (2010).

18. H. Hintiryan, N. N. Foster, I. Bowman, M. Bay, M. Y. Song, L. Gou, S. Yamashita, M. S. Bienkowski, B. Zingg, M. Zhu, X. W. Yang, J. C. Shih, A. W. Toga, H.-W. Dong, The mouse cortico-striatal projectome. *Nat. Neurosci.* **19**, 1100–1114 (2016).

19. B. J. Hunnicutt, B. C. Jongbloets, W. T. Birdsong, K. J. Gertz, H. Zhong, T. Mao, A comprehensive excitatory input map of the striatum reveals novel functional organization. *eLife* **5**, e19103 (2016).

20. J. M. Deniau, A. Menetrey, S. Charpier, The lamellar organization of the rat substantia nigra pars reticulata: Segregated patterns of striatal afferents and relationship to the topography of corticostriatal projections. *Neuroscience* **73**, 761–781 (1996).

21. D. Liu, W. Li, C. Ma, W. Zheng, Y. Yao, C. F. Tso, P. Zhong, X. Chen, J. H. Song, W. Choi, S.-B. Paik, H. Han, Y. Dan, A common hub for sleep and motor control in the substantia nigra. *Science* **367**, 440–445 (2020).

22. C. R. Lee, J. M. Tepper, Morphological and physiological properties of parvalbumin- and calretinin-containing gamma-aminobutyric acidergic neurons in the substantia nigra. *J. Comp. Neurol.* **500**, 958–972 (2007).

23. G. Rizzi, K. R. Tan, Synergistic nigral output pathways shape movement. *Cell Rep.* **27**, 2184–2198.e4 (2019).

24. L. Delgado-Zabalza, N. P. Mallet, C. Glangetas, G. Dabee, M. Garret, C. Miguelez, J. Baufreton, Targeting parvalbumin-expressing neurons in the substantia nigra pars reticulata restores motor function in parkinsonian mice. *Cell Rep.* **42**, 113287 (2023).

25. C. M. Gremel, D. M. Lovinger, Associative and sensorimotor cortico-basal ganglia circuit roles in effects of abused drugs. *Genes Brain Behav.* **16**, 71–85 (2017).

26. G. Sitzia, D. M. Lovinger, Circuit dysfunctions of associative and sensorimotor basal ganglia loops in alcohol use disorder: insights from animal models. *Addict Neurosci.* **5**, 100056 (2023).

27. L. H. Corbit, H. Nie, P. H. Janak, Habitual alcohol seeking: Time course and the contribution of subregions of the dorsal striatum. *Biol. Psychiatry* **72**, 389–395 (2012).

28. L. H. Corbit, H. Nie, P. H. Janak, Habitual responding for alcohol depends upon both AMPA and D2 receptor signaling in the dorsolateral striatum. *Front. Behav. Neurosci.* **8**, 301 (2014).

29. M. H. Patton, B. M. Roberts, D. M. Lovinger, B. N. Mathur, Ethanol disinhibits dorsolateral striatal medium spiny neurons through activation of a presynaptic delta opioid receptor. *Neuropsychopharmacology* **41**, 1831–1840 (2016).

30. T. Ma, Y. Cheng, E. Roltsch Hellard, X. Wang, J. Lu, X. Gao, C. C. Y. Huang, X.-Y. Wei, J.-Y. Ji, J. Wang, Bidirectional and long-lasting control of alcohol-seeking behavior by corticostriatal LTP and LTD. *Nat. Neurosci.* **21**, 373–383 (2018).

31. E. Roltsch Hellard, A. Binette, X. Zhuang, J. Lu, T. Ma, B. Jones, E. Williams, S. Jayavelu, J. Wang, Optogenetic control of alcohol-seeking behavior via the dorsomedial striatal circuit. *Neuropharmacology* **155**, 89–97 (2019).

32. R. Renteria, E. T. Baltz, C. M. Gremel, Chronic alcohol exposure disrupts top-down control over basal ganglia action selection to produce habits. *Nat. Commun.* **9**, 211 (2018).

33. R. Renteria, C. Cazares, E. T. Baltz, D. C. Schreiner, E. A. Yalcinbas, T. Steinkellner, T. S. Hnasko, C. M. Gremel, Mechanism for differential recruitment of orbitostriatal transmission during actions and outcomes following chronic alcohol exposure. *eLife* **10**, e67065 (2021).

34. R. Schmidt, D. K. Leventhal, N. Mallet, F. Chen, J. D. Berke, Canceling actions involves a race between basal ganglia pathways. *Nat. Neurosci.* **16**, 1118–1124 (2013).

35. M. A. Labouesse, A. Torres-Herraez, M. O. Chohan, J. M. Villarin, J. Greenwald, X. Sun, M. Zahran, A. Tang, S. Lam, J. Veenstra-VanderWeele, C. O. Lacefield, J. Bonaventura, M. Michaelides, C. S. Chan, O. Yizhar, C. Kellendonk, A non-canonical striatopallidal Go pathway that supports motor control. *Nat. Commun.* **14**, 6712 (2023).

36. W. M. Connelly, J. M. Schulz, G. Lees, J. N. J. Reynolds, Differential short-term plasticity at convergent inhibitory synapses to the substantia nigra pars reticulata. *J. Neurosci.* **30**, 14854–14861 (2010).

37. J. Brown, W.-X. Pan, J. T. Dudman, The inhibitory microcircuit of the substantia nigra provides feedback gain control of the basal ganglia output. *eLife* **3**, e02397 (2014).

38. K. M. Roman, A. R. Dinasarapu, A. VanSchoiack, P. M. Ross, D. Kroeppler, H. A. Jinnah, E. J. Hess, Spiny projection neurons exhibit transcriptional signatures within subregions of the dorsal striatum. *Cell Rep.* **42**, 113435 (2023).

39. Å. Wallén-Mackenzie, S. Dumas, M. Papathanou, M. M. Martis Thiele, B. Vlcek, N. König, Å. K. Björklund, Spatio-molecular domains identified in the mouse subthalamic nucleus and neighboring glutamatergic and GABAergic brain structures. *Commun. Biol.* **3**, 338 (2020).

40. D. Mallet, Cellular and synaptic dysfunctions in Parkinson's disease: Stepping out of the striatum. *Cells* **8**, 1005 (2019).

41. W. Shen, S. Zhai, D. J. Surmeier, Striatal synaptic adaptations in Parkinson's disease. *Neurobiol. Dis.* **167**, 105686 (2022).

42. J. Wang, Y. Cheng, X. Wang, E. Roltsch Hellard, T. Ma, H. Gil, S. Ben Hamida, D. Ron, Alcohol elicits functional and structural plasticity selectively in dopamine D1 receptor-expressing neurons of the dorsomedial striatum. *J. Neurosci.* **35**, 11634–11643 (2015).

43. Y. Cheng, C. C. Y. Huang, T. Ma, X. Wei, X. Wang, J. Lu, J. Wang, Distinct synaptic strengthening of the striatal direct and indirect pathways drives alcohol consumption. *Biol. Psychiatry* **81**, 918–929 (2017).

44. E. T. Baltz, R. Renteria, C. M. Gremel, Chronic alcohol exposure differentially alters calcium activity of striatal cell populations during actions. *Addict. Neurosci.* **8**, 100128 (2023).

45. M. V. Wilcox, V. C. Cuzon Carlson, N. Sherazee, G. M. Sprow, R. Bock, T. E. Thiele, D. M. Lovinger, V. A. Alvarez, Repeated binge-like ethanol drinking alters ethanol drinking patterns and depresses striatal GABAergic transmission. *Neuropsychopharmacology* **39**, 579–594 (2014).

46. V. C. Cuzon Carlson, G. K. Seabold, C. M. Helms, N. Garg, M. Odagiri, A. R. Rau, J. Daunais, V. A. Alvarez, D. M. Lovinger, K. A. Grant, Synaptic and morphological neuroadaptations in the putamen associated with long-term, relapsing alcohol drinking in primates. *Neuropsychopharmacology* **36**, 2513–2528 (2011).

47. V. C. Cuzon Carlson, K. A. Grant, D. M. Lovinger, Synaptic adaptations to chronic ethanol intake in male rhesus monkey dorsal striatum depend on age of drinking onset. *Neuropharmacology* **131**, 128–142 (2018).

48. L. DePoy, R. Daut, J. L. Brigman, K. MacPherson, N. Crowley, O. Gunduz-Cinar, C. L. Pickens, R. Cinar, L. M. Saksida, G. Kunos, D. M. Lovinger, T. J. Bussey, M. C. Camp, A. Holmes, Chronic alcohol produces neuroadaptations to prime dorsal striatal learning. *Proc. Natl. Acad. Sci. U.S.A.* **110**, 14783–14788 (2013).

49. B. Muñoz, B. M. Fritz, F. Yin, B. K. Atwood, Alcohol exposure disrupts mu opioid receptor-mediated long-term depression at insular cortex inputs to dorsolateral striatum. *Nat. Commun.* **9**, 1318 (2018).

50. D. L. Haggerty, B. Munoz, T. Pennington, G. Viana Di Prisco, G. G. Grecco, B. K. Atwood, The role of anterior insular cortex inputs to dorsolateral striatum in binge alcohol drinking. *eLife* **11**, e77411 (2022).

51. C. M. Gremel, R. M. Costa, Orbitofrontal and striatal circuits dynamically encode the shift between goal-directed and habitual actions. *Nat. Commun.* **4**, 2264 (2013).